

Final Draft
of the original manuscript:

Dieringa, H.; Huang, Y.; Wittke, P.; Klein, M.; Walther, F.;
Dikovits, M.; Poletti, C.:

**Compression-creep response of magnesium alloy DieMag422
containing barium compared with the commercial creep-resistant
alloys AE42 and MRI230D**

In: Materials Science and Engineering A (2013) Elsevier

DOI: 10.1016/j.msea.2013.07.041

**Compression-creep response of magnesium alloy DieMag422 containing barium
compared with the commercial creep-resistant alloys AE42 and MRI230D**

Hajo Dieringa^{1a}, Yuanding Huang^a, Philipp Wittke^b, Martin Klein^b, Frank Walther^b, Martina
Dikovits^c, Cecilia Poletti^c

^a Helmholtz-Zentrum Geesthacht, Centre for Materials and Coastal Research, MagIC –
Magnesium Innovation Centre, Institute for Material Research, Max-Planck-Straße 1, 21502
Geesthacht, Germany. hajo.dieringa@hzg.de, yuanding.huang@hzg.de

^b TU Dortmund, Faculty of Mechanical Engineering, Department of Materials Test
Engineering (WPT), Leonhard-Euler-Straße 5, 44227 Dortmund, Germany.
philipp.wittke@tu-dortmund.de, martin.klein@tu-dortmund.de, frank.walther@tu-
dortmund.de

^c Graz University of Technology, Institute for Materials Science and Welding,
Kopernikusgasse 24/I, 8010 Graz, Austria. martina.dikovits@tugraz.at,
cecilia.poletti@tugraz.at

¹ Corresponding author: Hajo Dieringa; Tel.: +49 4152 871955; Fax: +49 4152 871909; hajo.dieringa@hzg.de

Abstract

The development of creep-resistant magnesium alloys that avoid the use of rare-earth alloying elements is an important area of research. The creep response of Mg-Al-Ca alloy containing barium (DieMag422) was compared to that of commercially available creep resistant magnesium alloys AE42 and MRI230D. The creep tests were performed between 175°C and 240°C at stresses between 60 MPa and 120 MPa. From the temperature and stress dependence of the minimum creep rate, the apparent activation energy Q_c and the stress exponent n for creep were calculated. The concept of a threshold stress was applied. True stress exponents n_t close to 5 were calculated. Microstructural investigations and phase analysis were performed on the as-cast materials as well as after creep. Fine precipitates could be identified that justified application of the concept of threshold stress. The DieMag422 alloy shows an improvement in creep resistance at low stresses compared with the other two alloys AE42 and MRI230D.

Keywords: compression creep, magnesium alloys, barium, AE42, MRI230D, threshold stress

Introduction

There is a need to develop new creep-resistant and cheap magnesium alloys for automotive applications such as powertrains. Solid-solution strengthening, precipitation strengthening and the prevention of grain boundary sliding are the most common mechanisms used to improve creep resistance. The atomic radius of barium is 1.36 times larger than the magnesium atom, which suggests a high solid-solution strengthening ability. In Mg-Ba alloys, the Mg-Ba phases such as $Mg_{17}Ba_2$, $Mg_{23}Ba_6$ and Mg_2Ba have been reported [1-5]. Recent principle studies show that $Mg_{17}Ba_2$ and $Mg_{23}Ba_6$ are brittle phases whereas Mg_2Ba is ductile [4]. The

binary system Mg-Ba is modeled in [5] and the intermetallic compounds mentioned are consistent with experimental findings. There are various binary Al-Ba phases (AlBa , Al_2Ba , Al_4Ba , $\text{Al}_{13}\text{Ba}_7$, Al_5Ba_4) [6-12] existing in Al-Ba systems. The advantage of precipitates containing aluminium that may form during solidification is that they contribute to precipitation strengthening. In addition, the amount of β -phase $\text{Mg}_{17}\text{Al}_{12}$ may be limited, because the free aluminium prefers to form other precipitates. The β -phase is reported to be detrimental to the creep resistance of magnesium alloys containing aluminium [13, 14].

The addition of alkaline earth metals like Ca and Sr to magnesium alloys that are located in the same column as Ba in the periodic table of elements result in improvement of their creep resistance. The present work investigated the creep behaviour of Mg-Al-Ca alloy containing barium. Its creep properties are compared with that of AE42 and MRI230D alloys.

When a good creep resistance is desired in magnesium alloys containing aluminium, rare earths (RE) are often chosen as alloying elements, due to the formation of $\text{Al}_{11}\text{RE}_3$, Al_4RE and Al_2RE precipitates [15-17]. AE42 and AE44 are alloys that are used for high-temperature applications. A strong reason for wanting to replace rare-earth elements is because their primary production is concentrated in China, whose price development is uncertain. Creep resistant MRI230D alloy has already been investigated in terms of microstructure, phase identification and creep behaviour [18-20]. It was shown that it has a similar composition to AXJ520 and therefore $(\text{Mg}, \text{Al})_2\text{Ca}$ precipitates form that strengthen the alloy. Minimum creep rates found in tests under 110 MPa at 100°C and 180°C are very similar. The nominal composition of all three alloys investigated is given in Table 1.

Experimental

A magnesium alloy containing barium, DieMag422, was produced from a melt with highly purified magnesium (Mg-HP, >99.9%), pure aluminium (99.9%), barium (>99.0%) and

calcium (99.5%). The nominal composition is Mg-4Al-2Ba-2Ca. The temperature was kept constant at 720°C for ten minutes and the melt was stirred. AE42 and MRI230D are commercially available alloys. They were all melted and prepared in the same way. The alloys were cast in preheated rectangular moulds with a size of 150 x 200 x 20 mm³. The mould temperature was 300°C. A rising cast process was used in order to avoid turbulence during filling and dross in the solidifying part. After filling, the mould was cooled with water. The microstructure of each was examined using an optical microscope, a scanning electron microscope (SEM) and an electron transmission microscope (TEM). SEM investigations were performed using a Zeiss Ultra 55 equipped with an energy-dispersive X-ray analysis (EDX) system at an accelerating voltage of 15 kV. Additionally, a field emission gun (FEG) SEM FEI QUANTA 200 was used to characterize certain phases. Initially the specimens for TEM were ground mechanically to about 400 µm, and then discs of 3 mm diameter were cut using an abrasive-slurry disc cutter (Model 360, South Bay Technology, Inc). These discs were again mechanically ground to 120 µm, and further thinned by two-jet electro polishing using a solution of 1.5% HClO₄ and 98.5% ethanol at about -45°C and 40 V. The TEM examinations were carried out on a Philips CM 200 instrument operating at 200 kV. X-ray diffraction (XRD) investigations were carried out using Siemens diffractometer operating at 40 kV and 40 mA with Cu K α radiation. Measurements were obtained by step scanning from 20 to 120° with a step size of 0.02°. A count time of 3 seconds per step was used. The lattice parameters and space group were analyzed with the Rietveld refinement method using Software Topas 2.0.

Micro-hardness and macro-hardness tests were carried out using a Shimadzu Dynamic Ultra Micro-Hardness Tester DUH-211/S and a Wolpert Dia Testor 2RC, respectively. The load used for the hardness tests was 5 g (HV 0.005) and 10 kg (HV 10), respectively. Quantitative phase analyses were performed on SEM images by means of Phase-Fraction software from PixelFerber.

The compression tests of cylindrical specimens with an aspect ratio of 1.5 (dia: 10 mm; L₀: 15 mm) were carried out using a Gleeble[®]3800 device. The samples were deformed at 0.001 s⁻¹ strain rate in a temperature range of 20 to 240°C where the temperature was controlled by a K – thermocouple.

The cylindrical specimens with a diameter of 6 mm and a length of 15 mm for compression-creep tests were prepared by electrical discharge machining. The creep tests were performed with ATS Lever Testing Systems at a range of constant temperatures of 150°C, 175°C, 200°C and 240°C, and under constant stresses of 60, 70, 80, 100 and 120 MPa. 150 to 200°C is the temperature range typical for automotive powertrain components such as transmission cases [21]. The higher creep-test temperature of 240°C provides further information about possible changes in deformation mechanisms. The lower stresses chosen for compression creep of 60 to 100 MPa are service stresses that apply, for example, where parts of transmission cases are bolted. The stress of 120 MPa is again to provide information about changes in the deformation behaviour above service stress levels. The tests were stopped after reaching the minimum creep rate.

Results and discussion

Microstructural observations before creep and hardness

Fig. 1 shows the microstructure of the as-cast DieMg422 alloy that was obtained by light optical microscopy. The size of dendrites is about 70 μm. Two types of particles were found, with different morphologies distributed at the dendrites and at grain boundaries, one is lamellar and the other blocky. The SEM micrograph shows that the white blocky phase has a size of about 5 to 10 μm (Fig. 2). The lamellar phase has a thickness of about 1 to 3 μm. The EDX line-scan analysis indicates that the lamellar phase is enriched with Al and Ca, whereas Ba is not present here more than in the surrounding area (Fig. 3a). The ratio of Al to Ca is

close to 2, which is obtained by the statistical analysis of 20 EDX quantitative point measurements as shown in Fig. 3b. The plot of the atomic percentages of Al against Ca renders a fitting line with a slope of ratio 1.98 ± 0.22 . This value is almost identical to the intermetallic Al_2Ca ratio and thus it can be concluded that this lamellar phase is Al_2Ca . The XRD results also demonstrate that the phase Al_2Ca exists in the as-cast DieMag422 alloy (Fig. 4). For the white blocky phase, any error in its EDX quantitative analysis caused by the disturbance from the matrix magnesium should be very small, because the size of these particles is really big with a value of 5 to 10 μm . Monte Carlo simulations indicate that under an accelerating voltage of 15 kV the disturbance from the matrix magnesium is very small when the particle size is more than 2 μm . EDX analysis shows that the white blocky phase is possibly the ternary phase, which contains Mg, Al and Ba with very little Ca. Statistical investigation using an EDX 20-point analysis indicates that the composition of this phase is 80.2 at.% Mg, 11.5 at.% Al and 7.5 at.% Ba with only 0.7 at.% Ca, see Table 2. The standard errors obtained are 1.1 at.%, 0.8 at.% and 0.5 at.% for Mg, Al and Ba, respectively. This means that the quantitative results of the EDX point analysis are reproducible. This phase has the structural formula $\text{Mg}_{21}\text{Al}_3\text{Ba}_2$ based on these quantitative results. A preliminary Rietveld refinement analysis on the XED pattern obtained indicates that this phase has a space group of $P42_1/nm$ with lattice parameters $a = 0.5274 \text{ nm}$ and $c = 2.4677 \text{ nm}$.

A large amount of fine, homogeneously distributed precipitates is usually required for applying the threshold stress concept in creep tests. Platelet-like precipitates can be observed in the high resolution FEG-SEM (Fig. 5). Interaction with dislocations can be assumed in a sufficient manner with this distribution of platelets.

The measured macro-hardness of the as-cast DieMag422 alloy was about $51 \pm 2 \text{ HV } 10$. Table 3 shows the results of the micro-hardness tests and phase analyses. The average and standard deviation values are based on three measurements. The highest micro-hardness was determined in the $\text{Mg}_{21}\text{Al}_3\text{Ba}_2$ phase with $166 \pm 24 \text{ HV } 0.005$. The Al_2Ca phase has a micro-

hardness of about 95 ± 9 HV 0.005. The lowest micro-hardness of 59 ± 11 HV 0.005 was measured in the primary phase. The total phase fraction from the $Mg_{21}Al_3Ba_2$ and Al_2Ca phases was about $9.5 \pm 0.57\%$ and $6.6 \pm 0.40\%$, respectively.

Compression tests

As an estimation of stresses applied during compression-creep tests, the compression yield strength (CYS) at 0.001 s^{-1} strain rate was determined. Fig. 6 shows the CYS at room and creep-test temperatures. By definition, creep takes place at stresses below the yield strength and plastic deformation occurs due to thermally activated mechanisms. At stresses above the CYS creep deformation takes place as well, but it is accompanied by athermal, long-range deformation processes [22, 23]. Stresses applied during compression-creep tests can be above the CYS. However, it should be noted that in such cases the total deformation also includes long-range plastic deformation and not thermal creep deformation alone. This has to be taken into account when deformation mechanisms are to be determined by applying Norton-Arrhenius-plots. When stresses above the CYS are applied, activation energies are no longer suitable for identifying deformation mechanisms, due to the additional, long-range and athermal deformation, and so the minimum creep rates are higher and the resulting slope of log/log plots of minimum creep rate against applied stress increases. Thus these are called *apparent* activation energies.

Creep behaviour

The representative creep curves of the three alloys tested at 175°C and 100 MPa can be seen in Fig. 7. Fig. 7a shows the deformation as a function of time, which is the typical creep curve. After a rather short initial creep stage, a secondary stage is followed by a third creep stage where softening already takes place and finally failure occurs. Fig. 7b presents the variation of creep rate with time. Fig. 7c shows the creep rate as a function of deformation. It

can be seen that in all cases the minimum creep rate occurs between 5 and 10% of deformation.

Usually the dependence of the minimum creep rate $\dot{\epsilon}_s$ on temperature T and applied stress σ is given by the Norton-Arrhenius-Equation (Eq. 1)

$$\dot{\epsilon}_s = \frac{ADGb}{kT} \left(\frac{\sigma}{G} \right)^n \quad (\text{Eq. 1})$$

where A is a material dependent constant, G the shear modulus, b the Burgers vector, k the Boltzmann constant and n the stress exponent, which gives information about the rate-controlling deformation mechanisms during creep. D is the diffusion coefficient, and this can be expressed as:

$$D = D_0 \cdot \exp\left[-\frac{Q_c}{RT}\right]. \quad (\text{Eq. 2})$$

where D_0 is the frequency factor and Q_c the apparent activation energy for creep. The stress exponent n can be determined by plotting the minimum creep rates in a double logarithmic creep rate and stress field. Fig. 8a-d shows these plots at the different temperatures under which the creep tests were performed. The stress exponent value n varies between 7.4 and 11.7 for different alloys at the tested temperatures. Table 4 lists these values.

The existence of a threshold stress (or back stress) σ_{thr} was described for the precipitate and particle-hardened alloys. The interaction between dislocations and precipitates is assumed to be the origin of threshold stress, but different explanations exist for the details of this including the additional stress that is needed to bow the dislocation between the precipitates,

called Orowan stress [24], the stress required to detach a dislocation from an obstacle [25, 26] and the additional back stress required for climbing over an obstacle [27]. In order to introduce threshold stress σ_{thr} into the calculation, Eq. 1 is usually modified in such a way that the effective stress σ_{eff} replaces the applied stress σ :

$$\sigma_{eff} = \sigma - \sigma_{thr} \quad (\text{Eq. 3})$$

and so giving Eq. 4

$$\dot{\epsilon}_s = \frac{ADGb}{kT} \left(\frac{\sigma_{eff}}{G} \right)^{n_t} \quad (\text{Eq. 4})$$

Here n_t is the true stress exponent, which is calculated based on the concept of a threshold stress. Li and Langdon [28] described a method to calculate the threshold stress. A minimum creep rate of 10^{-10} s^{-1} was determined as the lowest measurable creep rate. It corresponds to a deformation strain of approximately 1% in 3 years. An extrapolation of double logarithmic plots of $\dot{\epsilon}_s$ over the applied stress σ to a value of 10^{-10} s^{-1} gives the threshold stress σ_{thr} . The calculated values for σ_{thr} are given in Table 5. With increasing temperature the threshold stress decreases. DieMag422 resulted in the highest threshold stresses and AE42 the lowest. By this method, the plots of minimum creep rates over effective stress σ_{eff} give the true stress exponent n_t as seen in Fig. 8e-h. Both the stress exponents n and true stress exponents n_t are given in Table 4.

To evaluate the apparent activation energy for creep, plots are drawn of the logarithm of minimum creep rate over $1/T$ according to Eq. 1 and 2 (Fig. 9). Q_c can be calculated from the slope. Table 6 shows the values for Q_c .

After applying the concept of threshold stress, the true stress exponents n_t are in a range that fits to the theoretical assumptions concerned with the deformation mechanisms. A value of $n=3$ is related to the viscous glide of dislocations [29-31], $n=5$ is related to dislocation climbing at high temperatures [29, 30, 32] and $n=7$ to dislocation climbing at low temperatures [33]. A value of $n=1$ is explained by diffusion-based deformation mechanisms [34, 35]. In [34] a linear dependence of secondary creep rate on stress was determined in high-purity aluminium near to the melting temperature. In [35] it was found in studies on pure, polycrystalline magnesium at high temperatures and low stresses below 2.5 MPa. Here no primary creep was detected and no visible slip lines were determined. AE42 alloy gives the values of n_t between 3.8 and 6.6 under all temperatures and dislocation climbing appears to be the rate-controlling deformation mechanism. Both the MRI230D and DieMag422 alloys show an increase of n_t with increasing temperature. For these dislocation glide is apparently the rate-controlling mechanism at 150°C, whereas at higher temperatures it is dislocation climbing.

At lower stresses all activation energies for creep are higher than the activation energy for the self diffusion of pure magnesium, which is $Q_{SD} = 135$ kJ/mol [36, 37]. The fluctuations of Q_c in a range between 140 and 168 kJ/mol can be attributed to the basal and non-basal glide as well as dislocation climbing. It can be seen by plotting the temperature-normalized minimum creep rate over the shear modulus-normalized applied stress in Fig. 10a that of all the tests AE42 alloy exhibits the worst creep resistance, whereas MRI230D is better and DieMag422 is the best, especially at low stresses. In Fig. 10b the temperature-normalized minimum creep rate is plotted over the normalized effective stress and in the higher stress ranges a true stress exponent n_t close to 5 can be estimated. This agrees well with investigations into the creep

response of AS21 alloy by Zhang [38]. Burgers vector $b = 3.21 \times 10^{-10}$ m and a shear modulus $G = 16.6 \text{ GPa} * (1 - 0.00049) * (T - 300)$ were taken from [39] for the normalization.

Microstructures after creep

Typical TEM micrographs are shown in Fig. 11. In general, high density dislocations were observed at the front of large particles after creep. When the sample creeps at 150°C and 100 MPa, the dislocations are mainly aligned on basal planes of the alpha-Mg matrix as shown in Fig. 11a. With the temperature increased to 175°C, most of the dislocations remain aligned on basal planes (Fig. 11c), but some dislocations are observed aligned on non-basal planes (Fig. 11b and d). Determinations of Burgers vector using the invisibility criteria indicate that those dislocations aligned on basal planes are $\langle a \rangle$ type dislocations in the sample creeps at 150°C and 100 MPa, and $\langle c \rangle$ or $\langle a + c \rangle$ type dislocations in the sample creeps at 175°C and 100 MPa. The dislocations aligned on non-basal planes are $\langle a \rangle$ type dislocations in the sample creeping at 175°C and 100 MPa. These results demonstrate that as the creep temperature increases it appears that more slip systems are operative. In addition, the curved $\langle a \rangle$ type dislocations on non-basal planes observed in the sample creeping at 175°C indicate that a cross-slip of dislocations occurs relatively easily.

According to these observations of creep deformation substructures, it seems that basal slip is dominant when the creep temperature is low. This indicates that dislocation glide may be the rate-controlling deformation mechanism. This conclusion agrees with that obtained by an analysis of stress exponents. As the creep temperature increases, more slip systems are activated and cross-slipping occurs. At the same time dislocation climbing may also take place. The presence of $\langle c \rangle$ or $\langle a + c \rangle$ type dislocations on the basal planes of the alpha-Mg matrix is considered as evidence for the occurrence of dislocation climbing [40]. Therefore,

dislocation climbing may have taken place during creep deformation at 175°C and 100 MPa. For the sample creeping at 175°C and 100 MPa, dislocation climbing may be the rate-controlling deformation mechanism. Furthermore, a pinning of dislocations by particles can be observed and this supports the use of the threshold stress concept.

The good creep resistance of as-cast alloy DieMag422 may be due to two factors. Firstly, with their large sizes the second phases may effectively hinder grain boundary sliding, and these large second phases may strengthen the matrix of alpha-magnesium as happens in the short fibre strengthening mechanism of composites. The dislocation clustering near these large particles was frequently observed during TEM investigations (Fig. 11b). These large particles are thermally stable, because they did not change during creep deformation. Secondly, at a relatively low creep temperature of 175°C, some fine precipitates are observed and mainly located near the dendritic and grain boundaries, where the alloying elements were previously segregated. During creep at such temperatures, which are close to the ageing temperatures (for magnesium alloys the ageing temperatures are normally in the range 170°C to 250°C), fine precipitates are possibly formed. TEM observations indicate that these fine precipitates can effectively pin the dislocations (Fig. 11d). Further TEM investigations will be needed to clarify the dynamic precipitations of these fine particles and their interactions with the dislocations.

Conclusions

Two phases are identified in a magnesium alloy DieMag422 containing barium with a nominal composition of Mg-4Al-2Ba-2Ca. One is a lamellar phase Al_2Ca with a volume fraction of 6.6% and the other is a blocky phase $\text{Mg}_{21}\text{Al}_3\text{Ba}_2$ having a volume fraction of 9.5%. These two phases are normally located at the dendrites and grain boundaries.

Creep response of DieMag422 was investigated and compared with conventional creep-resistant magnesium alloys AE42 and MRI230D. Threshold stresses of each alloy decrease with increasing temperature and DieMag422 shows the highest threshold stresses, which result in an excellent creep resistance. It can be concluded that with true stress exponents close to 5, dislocation glide at lower temperatures and dislocation climb at higher temperatures are the rate-controlling deformation processes. The activation energies for creep are always a little higher than the activation energy for self diffusion in pure magnesium.

Acknowledgement

The work was partially supported by the Austrian Agency of Research funds under the project number [P22238-N22]. The FEG-SEM device was provided by OSTEM in Vienna.

References

- [1] W. Klemm, F. Dinkelacker, *Z. Anorg. Chem.* 255 (1947) 2-12.
- [2] W.C. Zeek, PhD Thesis, Syracuse University (1956).
- [3] K.P. Anderko, *Trans. AIME* 209 (1957) 612-616.
- [4] Z. Yang, J. Du, B. Wen, C. Hu, R. Melnik, *Intermetallics* 32 (2013) 156-161.
- [5] X. Ren, C. Li, Z. Du, C. Guo, S. Chen, *Int. J. Mater. Res.* 104 4 (2013) 358-363.
- [6] E. Alberti, *Z. Metallkd.* 26 1 (1934) 6-9.
- [7] M. Iida, *J. Japan Inst. Metals* 17 (1953) 632-634.
- [8] G. Bruzzone, F. Merlo, *J. Less-Common Met.* 39 (1975) 1-6.
- [9] R.P. Elliot, F.A. Shunk, *Bull. Alloy Phase Diagrams* 2 3 (1981) 351-353.
- [10] S. Srikanth, K.T. Jacob, *Z. Metallkd.* 82 (1991) 675-679.

- [11] S. Srikanth, K.T. Jacob, *Met Trans.* 22B (1991) 607-616.
- [12] V.P. Itkin, C.B. Alcock, *J. Phase Equil.* 14 4 (1993) 518-524.
- [13] M. Regev, A. Rosen, M. Bamberger, *Met. Mat. Trans.* 32A (2001) 1335-1345.
- [14] D. Wenwen, S. Yangshan, M. Xuegang, X. Feng, Z. Min, W. Dengyun, *Mat. Sci. Eng. A356* (2003) 1-7.
- [15] B.R. Powell, V. Rezhets, M.P. Balogh, R.A. Waldo, *JOM* 54 (2002) 34-38.
- [16] A.A. Luo, *Int. Mat. Rev.* 49 1 (2004) 13-30.
- [17] P. Bakke, H. Westengen, S. Sannes, D. Albright, *SAE Techn. Paper* 2004-01-0655 (2004).
- [18] J.R. TerBush, R.R. Adharapurapu, J.W. Jones, T.M. Pollock, *Magnesium Technology 2009*, (2009) 161-165.
- [19] B. Backes, K. Durst, D. Amberger, M. Göken, *Met. Mat. Trans.* 40A (2009) 257-261.
- [20] J.R. TerBush, A. Suzuki, N.D. Saddock, J.W. Jones, T.M. Pollock, *Scr. Mat.* 58 (2008) 914-917.
- [21] M. O. Pekguleryuz, A. A. Kaya, *Adv. Engin. Mat.* 5 12 (2003) 866-878.
- [22] M. Celikin, F. Zanardi, D. Sediako, M.O. Pekguleryuz, *Can. Metall. Quart.* 48 4 (2009) 419-432.
- [23] M. Pekguleryuz, M. Celikin, *Int. Mat. Rev.* 55 4 (2010) 197-217.
- [24] E. Orowan, In: M. Cohen (Ed.), *Dislocation in Metals*, AIME, 1954.
- [25] E. Arzt, D.S. Wilkinson, *Acta Metall.* 34 10 (1986) 1893-1898.
- [26] E. Arzt, J. Rösler, *Acta Metall.* 36 4 (1988) 1053-1060.
- [27] E. Arzt, M.F. Ashby, *Scr. Metall.* 16 (1982) 1285-1290.
- [28] Y. Li, T.G. Langdon, *Scr. Mater.* 36 12 (1997) 1457-1460.
- [29] O.D. Sherby, P.M. Burke, *Prog. Mater. Sci.* 13 (1968) 325-389.

- [30] F.A. Mohamed, K.T. Park, E.J. Lavernia, *Mater. Sci. Eng.* A150 (1992) 21-35.
- [31] J. Weertman, *J. Appl. Phys.* 28 3 (1957) 362-364.
- [32] J. Weertman, *J. Appl. Phys.* 28 10 (1957) 1185-1189.
- [33] S.L. Robinson, O.D. Sherby, *Acta Mater.* 17 2 (1969) 109-125.
- [34] J. Harper, J.E. Dorn, *Acta Mater.* 5 11 (1957) 654-665.
- [35] S.S. Vagarali, T.G. Langdon, *Acta Met.* 29 (1981) 1969-1982.
- [36] J. Combronde, G. Brebec, *Acta Met.* 19 12 (1971) 1393-1399.
- [37] P.G. Shewmon, F.N. Rhines, *Trans. AIME* 200 (1954) 1021-1025.
- [38] P. Zhang, *Scr. Mat.* 52 (2005) 277-282.
- [39] H.J. Frost, M.F. Ashby, *Deformation Mechanism Maps*, Pergamon Press, Oxford 1982.
- [40] S. M. Zhu, J.F. Nie, M.A. Gibson, M.A. Easton, P. Bakke, *Met. Mat. Trans.* 43A (2012) 4137-4144.

Table 1: Nominal composition of the three alloys in wt.-%.

| Alloy | Al | RE* | Mn | Ba | Ca | Sr | Sn | Mg |
|-----------|-----|-----|------|----|-----|-----|------|------|
| AE42 | 4 | 2 | 0.3 | -- | -- | -- | | bal. |
| MRI230D | 6-7 | -- | <0.3 | -- | 2.1 | 0.3 | 0.84 | bal. |
| DieMag422 | 4 | -- | -- | 2 | 2 | -- | | bal. |

*RE: Rare-earth elements, usually a mixture (Mischmetal)

Table 2: EDX analysis on the white blocky phase in the as-cast DieMag422 alloy, indicating that this phase is $Mg_{21}Al_3Ba_2$.

| No. | Mg (at.%) | Al (at.%) | Ba (at.%) | Ca (at.%) |
|-----------------------|-------------|-------------|------------|------------|
| 1 | 79.84 | 11.78 | 7.79 | 0.59 |
| 2 | 81.64 | 10.34 | 7.10 | 0.91 |
| 3 | 82.04 | 9.70 | 7.67 | 0.59 |
| 4 | 81.00 | 10.60 | 7.88 | 0.52 |
| 5 | 80.32 | 11.41 | 7.75 | 0.53 |
| 6 | 79.64 | 12.01 | 7.82 | 0.53 |
| 7 | 80.14 | 11.42 | 7.88 | 0.56 |
| 8 | 79.54 | 12.01 | 7.93 | 0.52 |
| 9 | 78.83 | 12.47 | 6.99 | 1.70 |
| 10 | 80.12 | 12.18 | 7.29 | 0.41 |
| 11 | 80.50 | 11.74 | 7.34 | 0.41 |
| 12 | 80.16 | 11.45 | 7.79 | 0.59 |
| 13 | 80.38 | 11.34 | 7.75 | 0.53 |
| 14 | 80.52 | 11.10 | 7.89 | 0.49 |
| 15 | 76.99 | 13.36 | 6.27 | 3.38 |
| 16 | 79.59 | 12.10 | 7.81 | 0.50 |
| 17 | 79.55 | 12.05 | 7.83 | 0.57 |
| 18 | 81.31 | 10.96 | 7.25 | 0.48 |
| 19 | 79.98 | 11.70 | 7.76 | 0.55 |
| 20 | 81.80 | 11.16 | 6.61 | 0.43 |
| Average | 80.2 | 11.5 | 7.5 | 0.7 |
| Standard error | 1.1 | 0.8 | 0.5 | 0.7 |

Table 3: Micro-hardness and phase fractions of the different phases in the as-cast DieMag422 alloy.

| | Phase fraction [%] | Micro-hardness [HV 0.005] |
|--|--------------------|---------------------------|
| Primary phase | 83.9 ± 1.35 | 59 ± 11 |
| Al ₂ Ca | 6.6 ± 0.40 | 95 ± 9 |
| Mg ₂₁ Al ₃ Ba ₂ | 9.5 ± 0.57 | 166 ± 24 |

Table 4: Stress exponent n and true stress exponent n_t from double logarithmic plots of minimum creep rate over applied stress and effective stress, respectively.

| Alloys | stress exponent n | | | | true stress exponent n_t | | | |
|-----------|---------------------|-------|-------|-------|----------------------------|-------|-------|-------|
| | 150°C | 175°C | 200°C | 240°C | 150°C | 175°C | 200°C | 240°C |
| AE42 | 9.2 | 9.4 | 9.3 | 8.6 | 3.8 | 5.1 | 5.9 | 6.6 |
| MRI230D | 8.8 | 9.2 | 8.2 | 7.4 | 2.5 | 4.4 | 5.2 | 5.8 |
| DieMag422 | 9.3 | 11.4 | 11.7 | 8.7 | 2.2 | 3.7 | 5.4 | 6.3 |

Table 5: Threshold stress σ_{thr} of all alloys at the different test temperatures.

| Alloys | Threshold stress σ_{thr} [MPa] at | | | |
|-----------|--|-------|-------|-------|
| | 150°C | 175°C | 200°C | 240°C |
| AE42 | 45.9 | 36.6 | 29.5 | 19.1 |
| MRI230D | 54.1 | 42.0 | 30.5 | 18.3 |
| DieMag422 | 56.2 | 51.1 | 43.1 | 23.0 |

Table 6: Apparent activation energy for creep from plots of minimum creep rate over $1/T$.

| Alloys | Activation energy Q_c [kJ/mol] | | | | |
|-----------|----------------------------------|--------|--------|---------|---------|
| | 60 MPa | 70 MPa | 80 MPa | 100 MPa | 120 MPa |
| AE42 | 141.7 | 143.3 | 153.5 | 152.6 | 127.9 |
| MRI230D | 162.9 | 148.9 | 151.1 | 145.0 | 137.0 |
| DieMag422 | 146.0 | 168.0 | 160.2 | 151.5 | 144.4 |

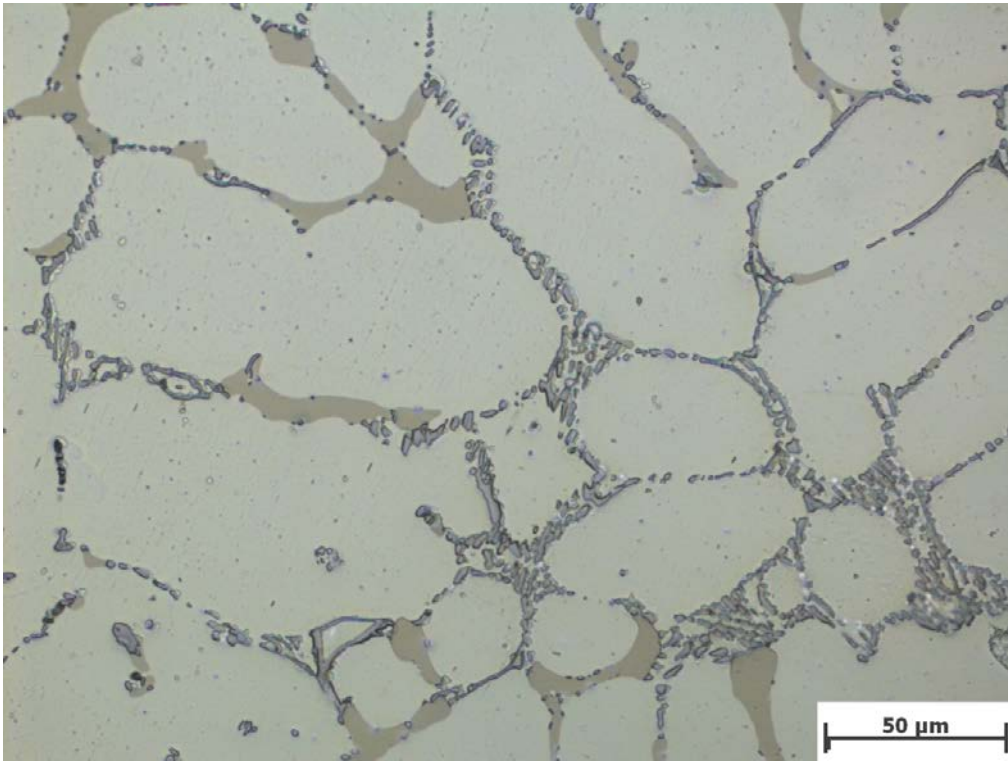


Fig. 1: Light-optical microstructure of the as-cast DieMag422 alloy.

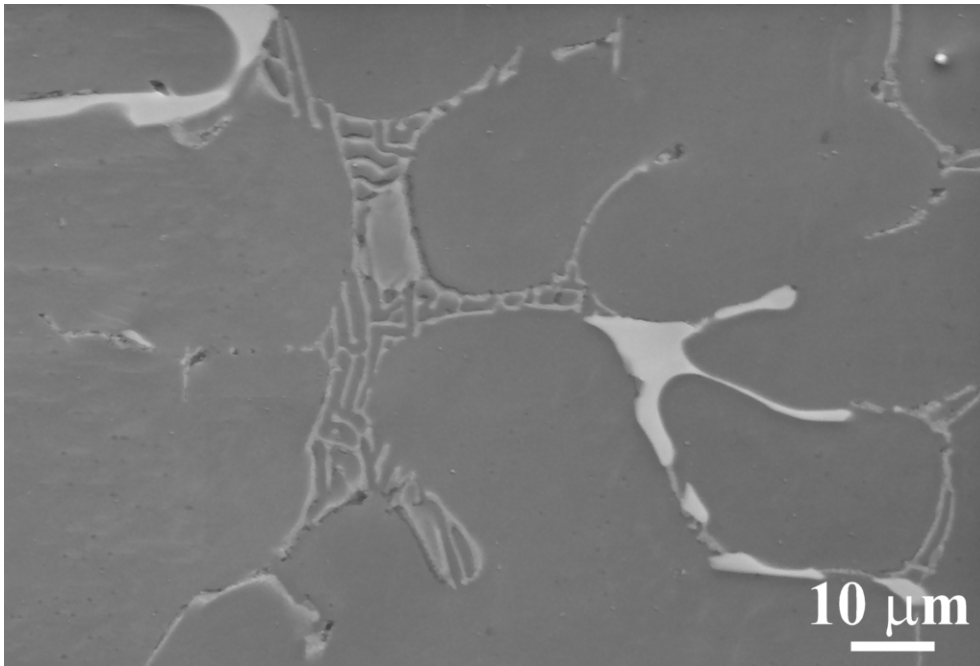


Fig. 2: SEM micrograph showing the morphologies of second phases in the as-cast DieMag422 alloy.

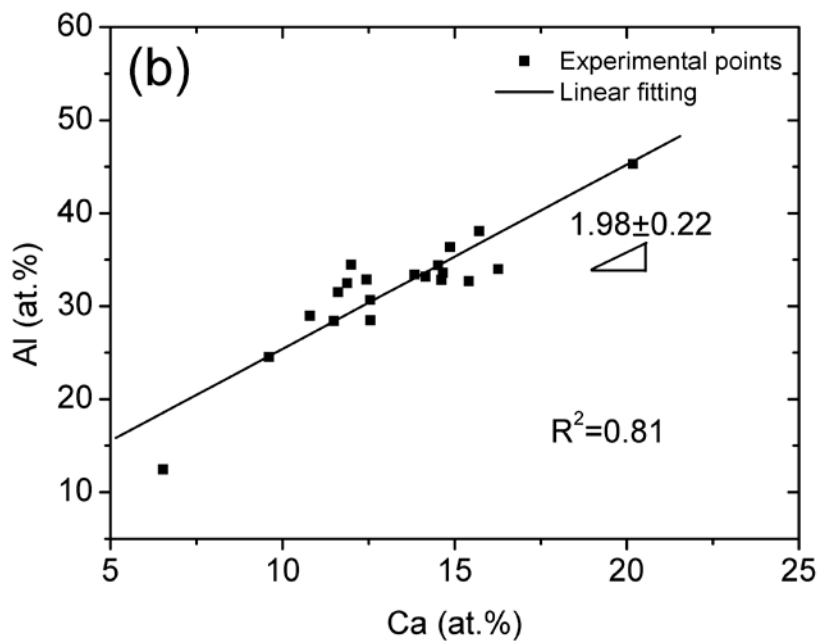
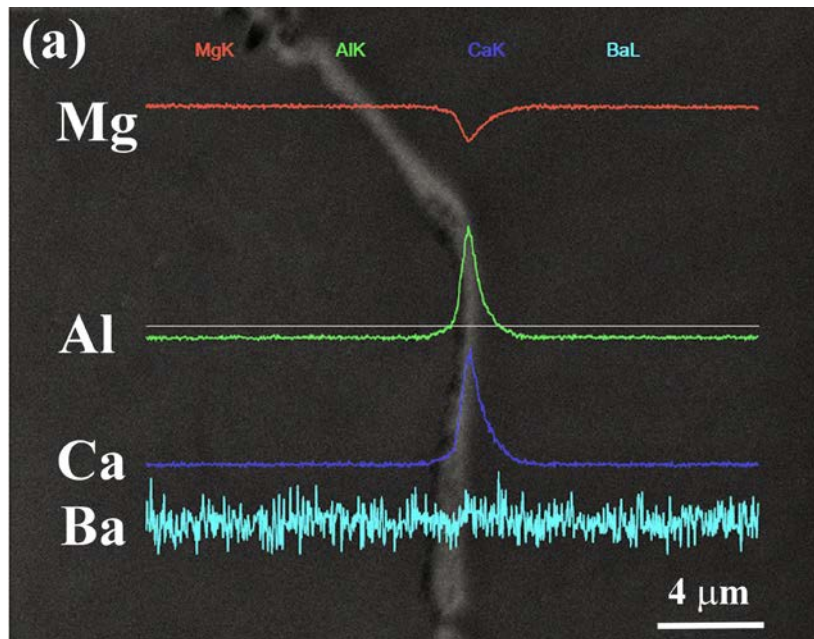


Fig. 3: EDX analysis on the grey lamellar phase in the as-cast DieMag422 alloy, (a) line scan analysis, no Ba enrichment is observed; (b) 20-point analysis showing the ratio of Al to Ca is close to 2. The results shown in these two plots indicate that this phase could be Al_2Ca .

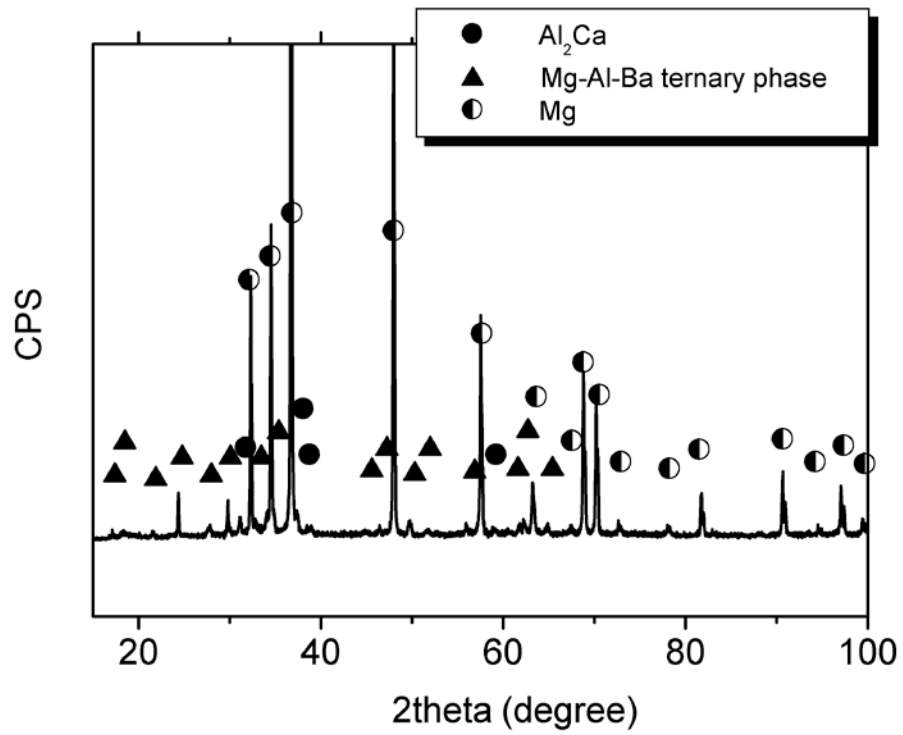


Fig. 4: XRD pattern of the as-cast DieMag422 alloy. Three phases are identified: Mg, Al_2Ca and Mg-Al-Ba ternary phase.

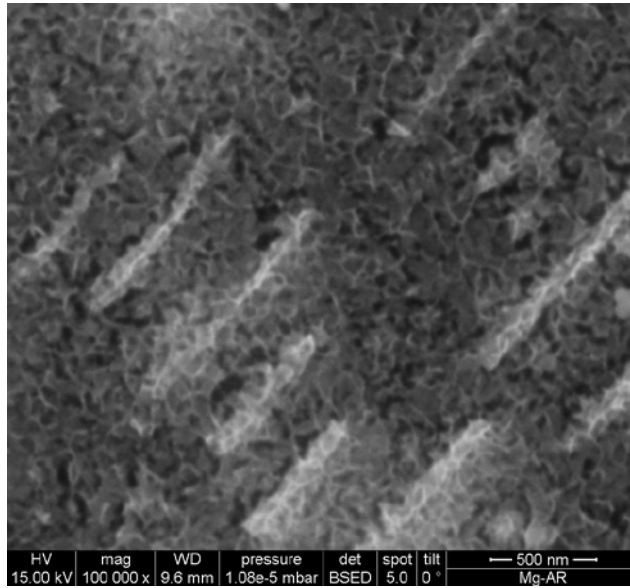


Fig. 5: FEG-SEM image in high resolution of platelet-like precipitates.

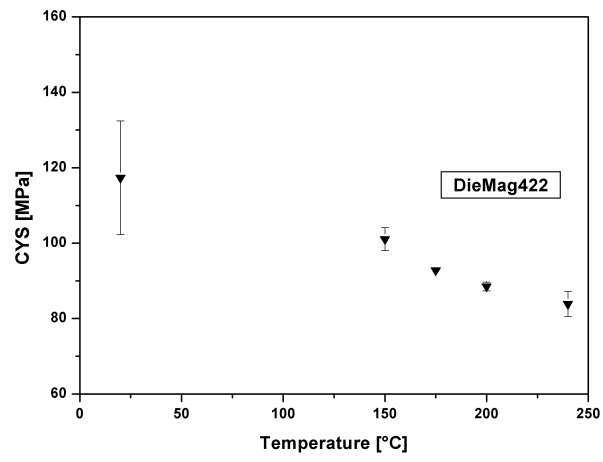


Fig. 6: Compressive yield strength at 0.001 s^{-1} strain rate of alloy DieMag422.

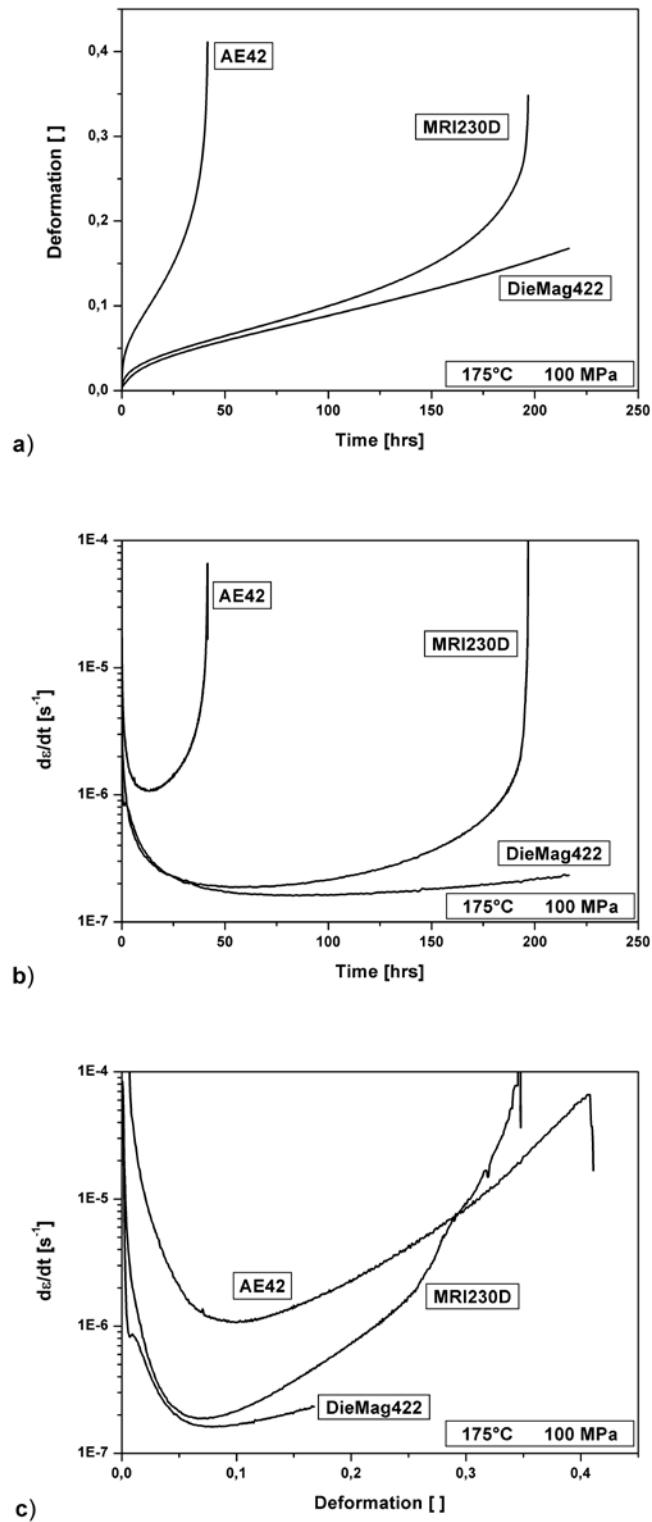


Fig. 7: Creep curves of tests performed at 175°C and 100 MPa, (a) deformation as a function of time; (b) creep rate as a function of time; (c) creep rate as a function of deformation.

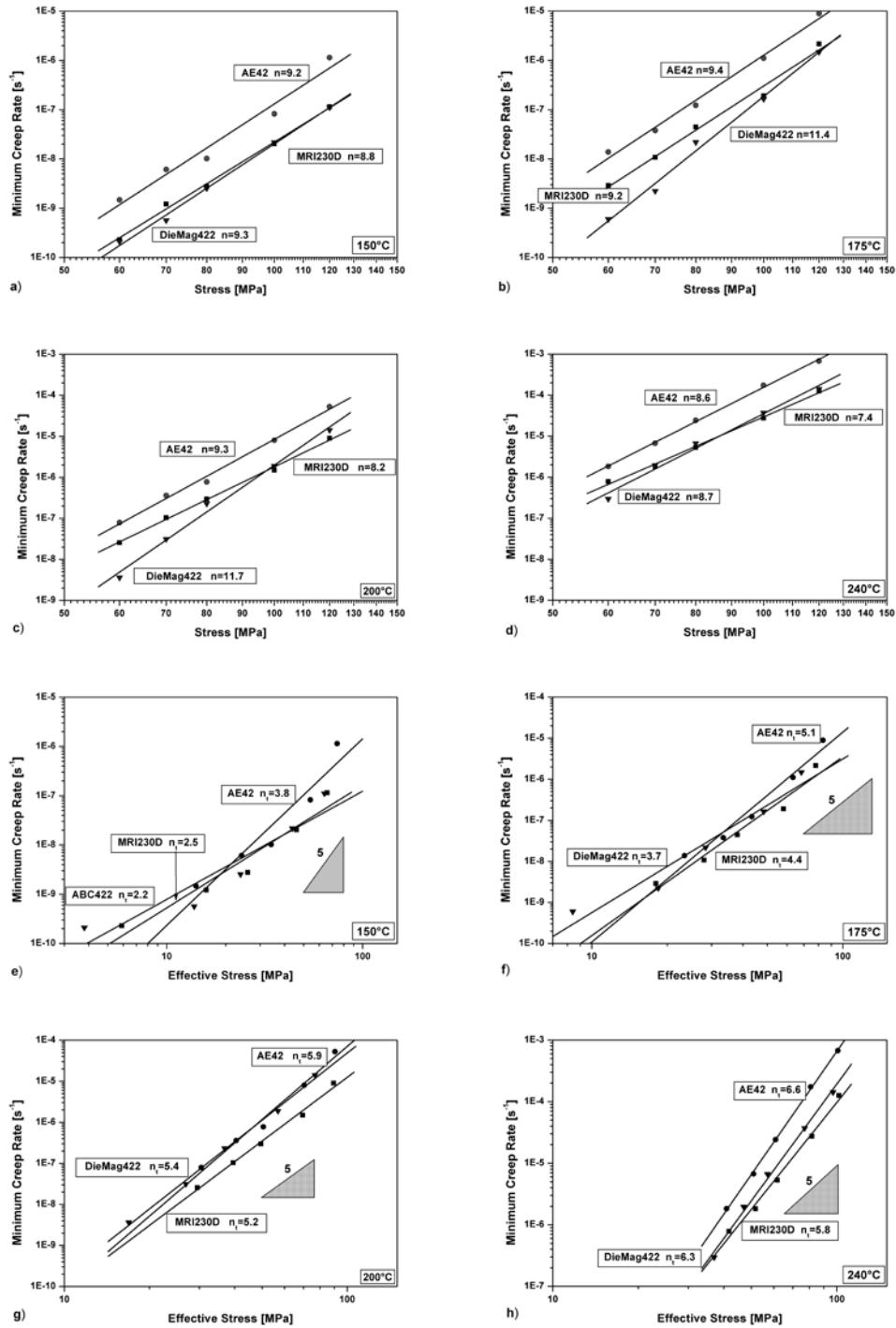


Fig. 8: Minimum creep rates depending on the applied stress of creep tests, at (a) 150°C, (b) 175°C, (c) 200°C and (d) 240°C. Linear fits of slopes give each a stress exponent n . Minimum creep rates dependant on the effective stress of creep tests, at (e) 150°C, (f) 175°C, (g) 200°C and (h) 240°C. The linear fits of slopes give each a true stress exponent n_t .

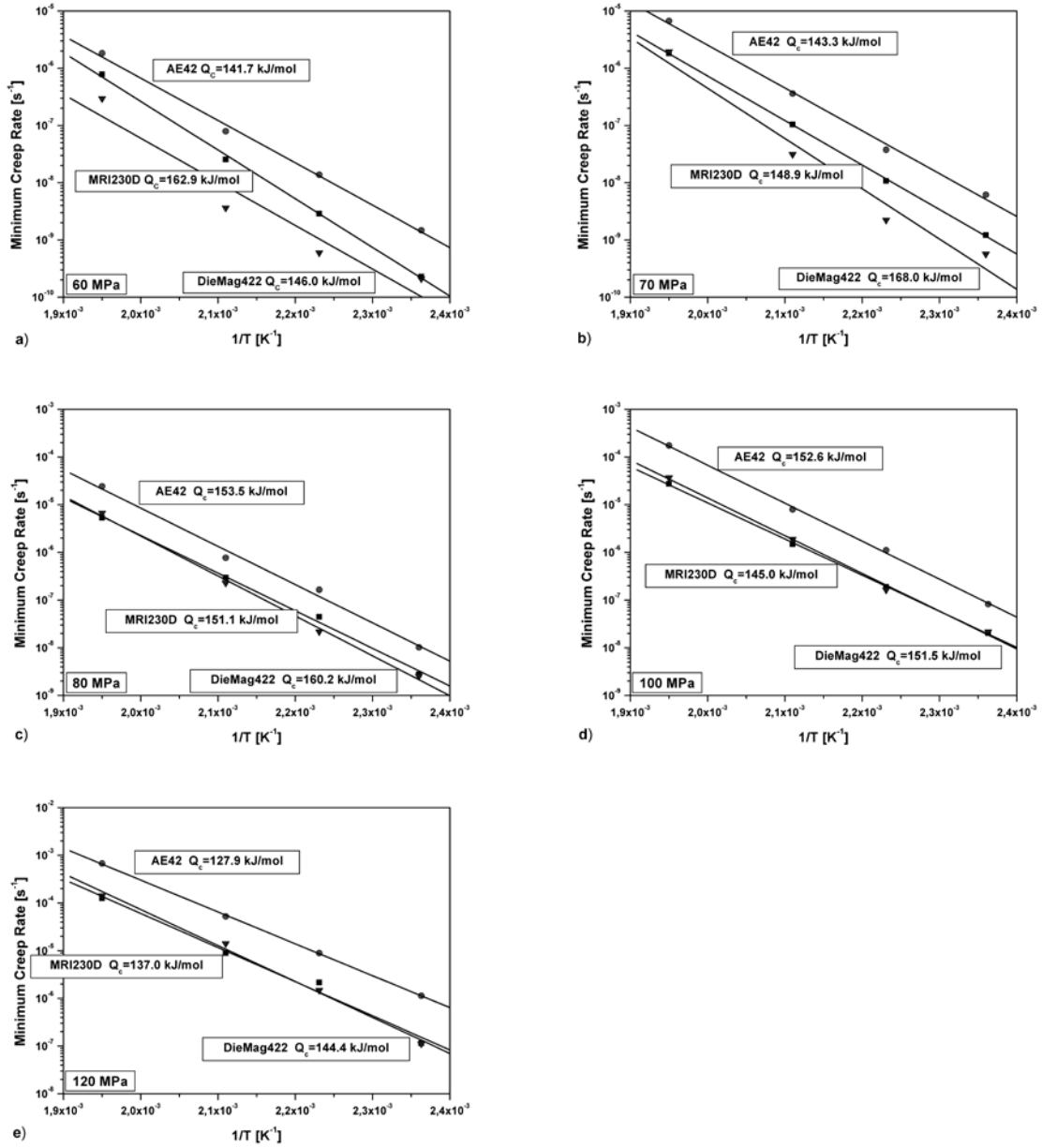


Fig. 9: Minimum creep rates dependant on the inverse temperature of creep tests. at (a) 60 MPa, (b) 70 MPa, (c) 80 MPa, (d) 100 MPa, and (e) 120 MPa. The linear fits of slopes give the apparent activation energy for creep Q_c .

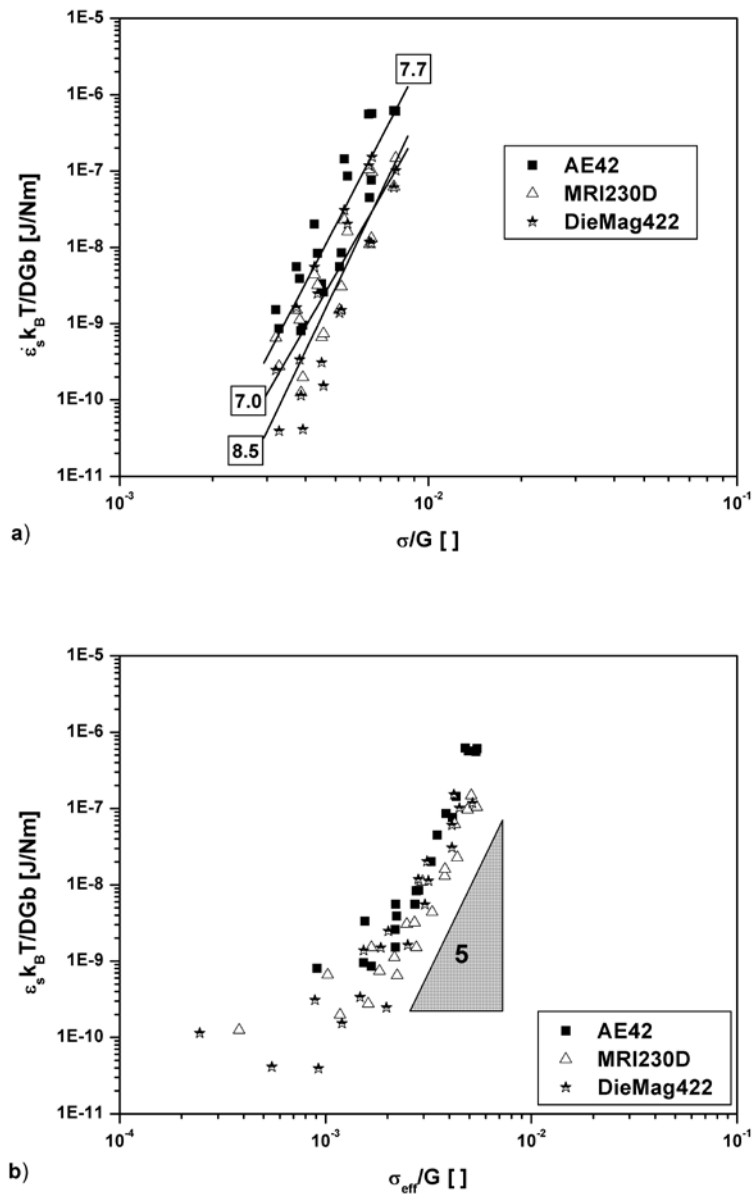


Fig. 10: Temperature-normalized minimum creep rate over (a) the shear modulus normalized applied stress, and (b) the shear-modulus-normalized effective stress.

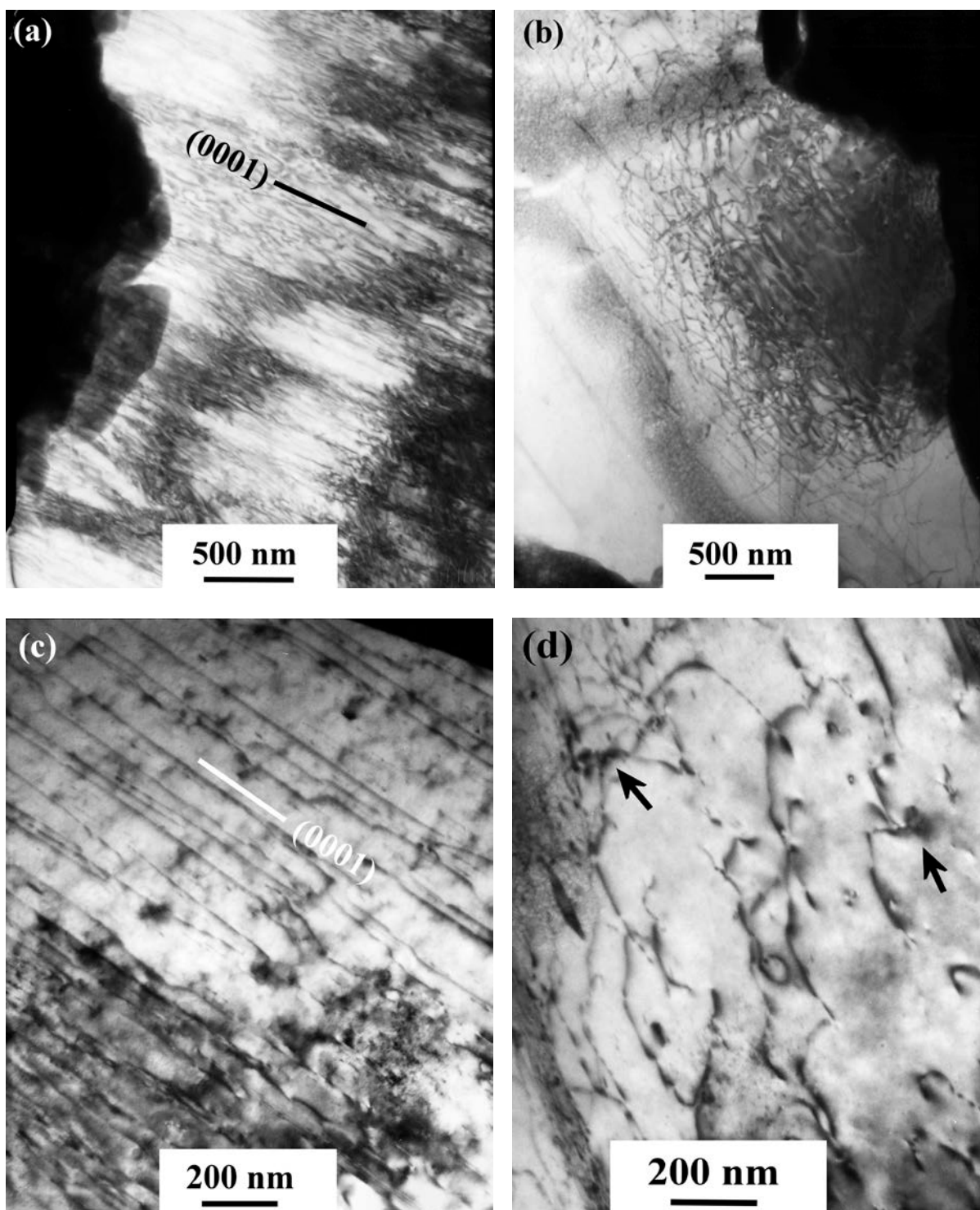


Fig. 11. TEM pictures show the microstructures after creep from: (a) creeping at 150°C and 100 MPa; (b) creeping at 175°C and 100 MPa; (c) creeping at 175°C and 100 MPa; (d) creeping at 175°C and 100 MPa.